Sensors and Actuators A 298 (2019) 111564

Contents lists available at ScienceDirect

Sensors and Actuators A: Physical

journal homepage: www.elsevier.com/locate/sna

A micromachined water-immersible scanning mirror using BoPET hinges

Song Xu, Shuangliang Li*, Jun Zou

Department of Electrical and Computer Engineering, Texas A&M University, College Station, TX, 77843, USA

ARTICLE INFO

Article history:
Received 12 June 2019
Received in revised form 4 August 2019
Accepted 17 August 2019
Available online 19 August 2019

Keywords:
Water-immersible
Two-axis scanning mirror
Polymer hinges
Plasma etching
Miniaturization

ABSTRACT

This paper reports a new micromachined two-axis water-immersible scanning mirror using BoPET (biaxially-oriented polyethylene terephthalate) hinges. A new fabrication process based on deep plasma etching on a hybrid silicon-BoPET substrate was developed to enable high-resolution patterning and batch fabrication capability. For demonstration, a prototype scanning mirror was designed, fabricated and tested. It has an overall size of $5 \times 5 \times 5\,\text{mm}^3$, which is comparable to that of a typical silicon-based micro scanning mirror. With a short-hinge design, the size of the mirror plate reaches $4 \times 4\,\text{mm}^2$ to provide an even larger aperture for optical or acoustic beam steering. In the air, the resonance frequencies of the fast and slow axes are 420 Hz and 190 Hz respectively. When immersed in water, the resonance frequencies are reduced to 330 Hz and 160 Hz, respectively. The tilting angles of the mirror around the fast and slow axes follow a linear relationship with the driving current up to $\pm 3.5^\circ$. With both axes driven simultaneously, stable and repeatable raster scanning patterns were obtained in both air and water. The micromachined water-immersible scanning mirrors could be useful for various scanning optical and acoustic microscopic imaging applications in both air and liquid environments.

1. Introduction

RECENTLY, new scanning mirrors have been developed and operated in water to provide enlarged scanning angles (based on the Snell's law) [1] or fast co-scanning of focused optical and ultrasound beams [2,3]. Different from conventional silicon-based scanning mirrors [4–7], torsional hinges made of flexible and high-strength thick BoPET (biaxially-oriented polyethylene terephthalate) films were used to avoid possible shock damage in water [8,9]. However, due to the excellent chemical stability of BoPET, high-resolution patterning of the BoPET hinges still poses a challenge. Previously, different methods for BoPET patterning have been studied, including CO_2 laser cutting or excimer laser ablation [10,11] and oxygen plasma etching [12]. Although it can achieve a high cutting speed and a depth of several millimeters, the CO_2 laser cutting has low lateral resolution of a few hundred microns. The excimer laser ablation can achieve very high spatial resolution. However, its serial nature limits the cutting speed and overall throughput, which makes it unsuitable for batch fabrication. Oxygen plasma etching could provide a practical solution for BoPET patterning [12]. However, the etch rate achieved so far is low, which makes the plasma etching process mainly useful for thin-film patterning. As a result, current fabrication process for the water-immersible scanning mirror with BoPET hinges still relies on laser cutting and mechanical dicing followed by multiple steps of manual assembly. It is a serial process with low spatial resolution and alignment accuracy, which prevents the miniaturization and batch fabrication of the mirror modules [13].

In this paper, we report a new micromachined water-immersible scanning mirror using BoPET hinges. The overall size of the mirror package was reduced down to $5 \times 5 \times 5\,\text{mm}^3$ (from $10 \times 10 \times 15\,\text{mm}^3$ with previous fabrication process [13]), which is on par with a typical silicon-based micro scanning mirror. To achieve this, a new deep plasma etching process on hybrid BoPET-silicon substrates has been developed and characterized. It can achieve high spatial resolution and reasonable etch rates and significantly reduce the number of manual assembly steps, making the miniaturization and batch fabrication of possible. In addition, it also allows several technical performance improvements over previously-fabricated mirror modules. First, with a smaller mirror structure, higher scanning frequency can be achieved; Second, due to much higher patterning resolution (e.g., a few microns vs. 100 s of microns), the dimension of the mirror structures can be precisely defined to facilitate performance tuning and control.

* Corresponding author.
E-mail addresses: xssong@tamu.edu (S. Xu), slli940922@tamu.edu (S. Li), junzou@tamu.edu (J. Zou).

https://doi.org/10.1016/j.sna.2019.111564
0924-4247/

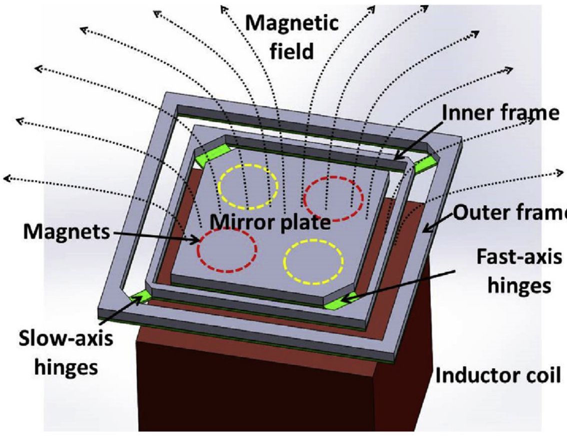

Fig. 1. Schematic Design of the Two-Axis Water-Immersible Scanning Mirror.

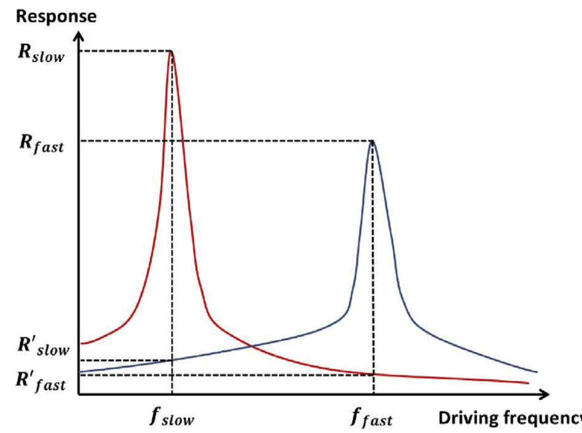

Fig. 2. Dynamic filtering effect.

Third, with better alignment accuracy and less steps of manual assembly, more uniform scanning performances can be expected. For demonstration, a prototype scanning mirror was designed, fabricated and tested. The small footprint of the micromachined water-immersible scanning mirror makes it suitable for the development of compact ultrasound and photoacoustic imaging systems for handheld, head-mounted, and even endoscopic applications.

2. Design

Fig. 1 shows the schematic design of the two-axis water-immersible scanning mirror. The mirror plate is supported onto the inner frame by two BoPET hinges (to form the fast axis). The inner frame and the outer frame are connected by the other two BoPET hinges (to form to the slow axis). Compared with the brittle silicon hinges used in conventional MEMS scanning mirrors, the BoPET hinges are more flexible and impact resistant. Therefore, they are suitable for under-water operations where shock or turbulence could occur. In addition, the low Young's modulus (2–2.7 GPa [14]) and high flexibility of BoPET makes it possible to achieve desirable torsion stiffness and scanning angle without using long and slender hinge structures. This brings two benefits: 1) More efficient usage of the mirror surface area. With shorter hinges, the gap between the mirror plate and frames can be reduced. Larger mirror plate can be accommodated without increasing the overall module size; 2) Better suppression of the vertical vibration of the mirror plate. As the first-order estimation, the bending and torsion force constants of a micro cantilever beam can be calculated as

$$k_{bending} = \frac{3EI}{l^3} = \frac{Ewt^3}{4l^3} \quad (1)$$

$$k_{torsion} = \frac{GJ}{l} = \frac{Gwt^3[\frac{16}{3} - 3.36\frac{t}{w}(1 - \frac{t^4}{12w^4})]}{l} \quad (2)$$

Where, E is Young's modulus, I is moment of inertia, J is torsional moment of inertia, and G is shear modulus. Suppose the beam width and thickness are kept constant, the ratio between the bending and torsion force constants as a function of the beam length can be determined as

$$\frac{k_{bending}}{k_{torsion}} = \frac{2(1+\upsilon)}{4l^2[\frac{16}{3} - 3.36\frac{t}{w}(1 - \frac{t^4}{12w^4})]} \quad (3)$$

Where, υ is Poisson's ratio. According to Eq. (3), the ratio between the bending and torsion force constants increases with $1/l^2$. For given torsion stiffness, a shorter hinge will have much higher bending stiffness and can better suppress the vertical vibration caused by environmental disturbance or unbalanced driving forces.

To drive both fast and slow axes, a water-compatible electromagnetic actuator is used [13], which consists of two pairs of permanent magnets (marked in red and yellow) and one inductor coil. In each pair, the two magnets are inversely magnetized and attached to the backside of the mirror plate. When a current is flowing through the inductor coil, a magnetic torque will be generated to rotate the mirror plate around the fast-axis hinges and also the inner frame around the slow-axis hinges. The use of single inductor (instead of multiple ones) to drive both the fast and slow axes can result in a significant reduction of the mirror module size. However, the scanning motion around the two axes is mechanically coupled and cannot be independently controlled.

To address this issue, we have investigated a dynamic filtering effect to enable independent two-axis driving with a single inductor coil [13]. As shown in Fig. 2, the resonance frequency of the fast axis (f_{fast}), is made much higher than that of the slow axis (f_{slow}). When two AC driving currents with different frequencies (f_{fast} and f_{slow}) are passed through the inductor coil, the fast and slow axes will be driven simultaneously by the two currents. The scanning motion of the fast and slow axes can be represented by $R_{fast} + R'_{slow}$ and $R_{slow} + R'_{fast}$, respectively. When f_{fast} and f_{slow} are separate far enough, $R_{fast} \gg R'_{slow}$ and $R_{slow} \gg R'_{fast}$. As a result, the coupled responses (R'_{fast} and R'_{slow}) will become negligible when compared with the actuated responses (R_{fast} and R_{slow}). Capitalizing upon this intrinsic dynamic filtering effect, the coupling between the two axes can be largely suppressed to allow independent control of the two scanning motions even with a single inductor coil.

To make the resonance frequencies of the two scanning axes significantly different, the fast-axis hinges are designed to be both wider and shorter than slow-axis hinges to provide a larger torsional constant. At the same time, the area of the inner frame is enlarged to increase moment of inertia around the slow axis to further reduce its resonance frequency. It should be mentioned that due to the low Young's modulus and high flexibility of BoPET, a wide range of dimensions (both length and width) can be chosen to provide desirable mechanical stiffness for the fast- and slow-axis hinges.

Table 1 lists the main design parameters of the scanning mirror. For verification, the scanning behavior of both fast and slow axes was simulated in COMSOL Multiphysics®. The AC/DC module was used to calculate the magnetic fields from the inductor coil and permanent magnets and the resulting magnetic forces. The coil was set to be homogenized and numerical with an estimated number of turns of $\tilde{5}000$. The magnetic flux from the coil was calculated from the driving current. Permanent magnets were simulated by the Ampere's Law. After selecting the domain, the magnetic field was defined by remnant flux density, $B_r = 0.3$ Tesla.

Table 1
Main Design Parameters of the Two-Axis Water-Immersible Scanning Mirror.

	Fast-axis	Slow-axis
Hinge (l × w × t) (mm^3)	0.4 × 0.56 × 0.05	0.7 × 0.2 × 0.05
Rotational part (mm^2)	4 × 4	4.5 × 4.5
	BoPET film [14]	
Shear modulus (GPa)	0.02	
Density (ρ_c) (g/cm^3)	1.455	
	Inductor Coil	
Inductance (μH)	1	
Length/diameter (mm^2)	2 × 3	
Estimated number of turns	5100	
	Permanent magnet	
Diameter/height (mm^2)	1.5 × 0.7	
Density (g/cm^3)	7.5	
Remanent flux density (T)	0.3	

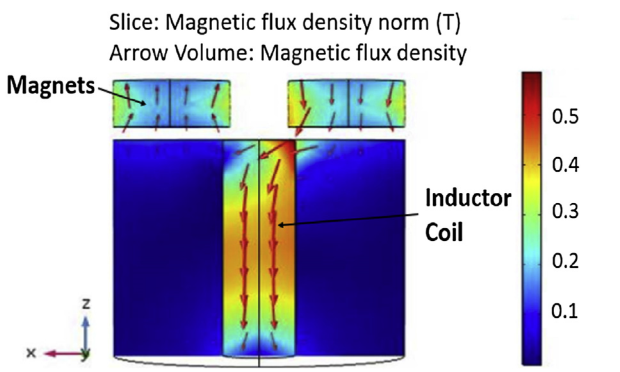

Fig. 3. Simulated magnetic flux density distribution of the inductor coil and permanent magnets.

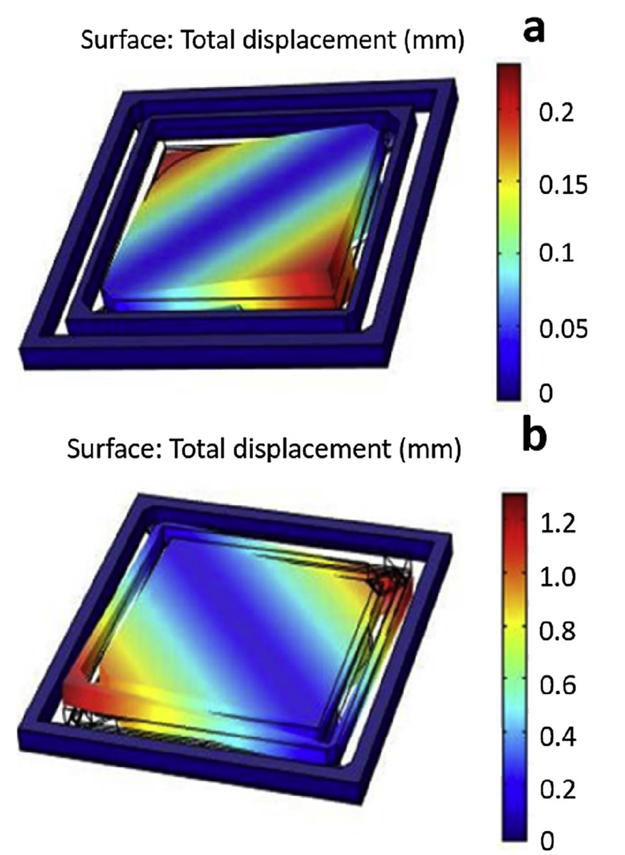

Fig. 4. Simulated vertical displacement of the mirror plate around the (a) fast axis and (b) slow axis.

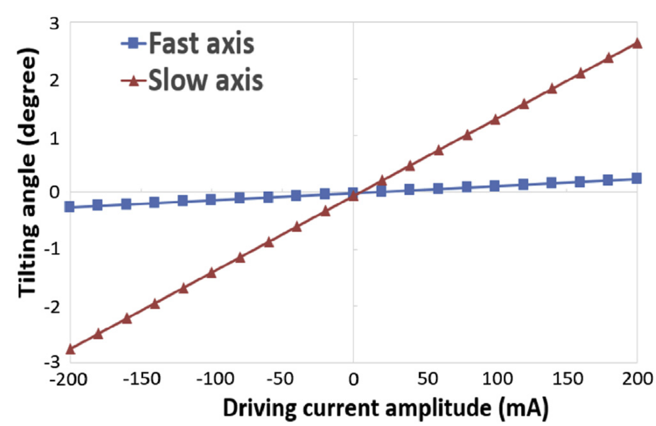

Fig. 5. Simulated DC driving responses.

Combining the magnetic fields generated by inductor coil and magnetic fields introduced by permanent magnets (Fig. 3), the magnetic forces applied onto the mirror plate were determined. Next, with the Structural Mechanics module, the magnetic forces were applied to calculate the tilting angles of the mirror plate (Fig. 4).

The tilting angles of the mirror plate around the two axes under DC driving conditions were determined by applying DC driving currents with different amplitude. As shown in Fig. 5, linear relationship between the driving signal amplitudes and tilting angles was observed. At small tilting angles, the gap between the inductor coil and the permanent magnets changes only slightly. As a result, the magnetic forces can remain almost constant for a certain DC driving current. However, at larger tilting angles, non-linearity can be expected as the magnetic forces start to diminish when the gap between the inductor coil and permanent magnets increases. The tilting angle of the slow axis increases faster than that of the fast-axis, which is due to its lower stiffness. This means a smaller driving current for the slow axis will be needed to generate the same tilting angle as that of the fast axis. This is helpful for enhancing the dynamic filtering by reducing the mechanical coupling to the fast axis.

To calculate the resonance frequencies of the fast and slow axes in the air and water, the driving signal frequency was swept from 1 Hz to 1 kHz, (Fig. 6). Around the resonance frequency, the step of the frequency sweep was set to the minimal value of 1 Hz. The resonance frequency was defined as at which frequency the scanning angle reaches its maximum. The resonance frequencies of the fast and slow axes in the air were determined to be 445 Hz and 179 Hz, respectively. When immersed in water, the resonance frequencies were reduced to 367 Hz and 151 Hz, respectively. In both cases, the resonance frequency of the fast axis is at least twice of that of the slow axis to ensure the validity of the dynamic filtering effect. For scanning optical and acoustic microscopy, the repetition rate of laser or ultrasound pulses is usually 10Ĩ00 kHz. To maintain high density of data points for good image resolution, the scanning frequencies of the fast and slow axes should be 10s–100 s Hz. Therefore, the above resonance frequencies of the scanning mirror are suitable for such applications.

3. Fabrication and assembly

As discussed in the introduction, the main issues in current plasma etching processes for BoPET are low etch rates and poor aspect ratio, which make it difficult for deep etching in thick substrates. In plasma etching of polymer materials, oxygen is the main reaction gas. However, with the presence of high oxygen concentration in the plasma, the side-wall protection with polymer film

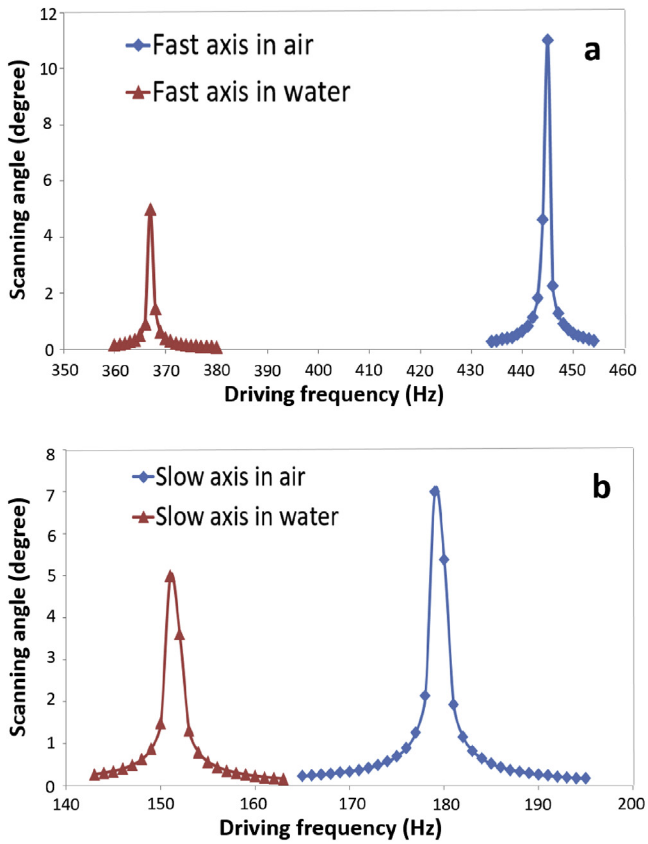

Fig. 6. Resonance frequency simulation results of (a) the fast axis and (b) the slow axis.

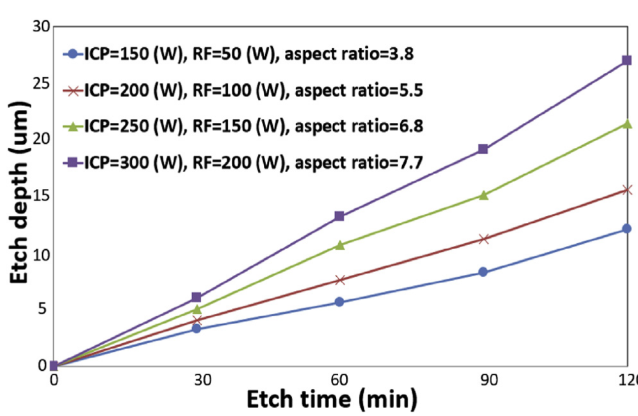

Fig. 7. Etching results with different ICP and RF power levels.

formation, which is commonly used in deep silicon etching, will become ineffective. To obtain good aspect ratio, high-energy bombardment is needed to enhance the anisotropic physical etching. In this work, a gas mixture consisting of argon and oxygen (3:1) was used to provide a good balance of physical and chemical etching [15]. Using the same gas mixture, the etch rate and aspect ratio of BoPET under different ICP (inductive coupled plasma) and RF (radio frequency) power levels were characterized. As shown in Fig. 7, both the etch rate and aspect ratio increase with the ICP and RF power as a result of enhanced bombardment of ions with higher density and energy. However, if the ICP and especially the RF power are too high, the BoPET substrate can be overheated, which causes wrinkling and degradation of its mechanical properties. In this work, an ICP power of 300 W and an RF power of 200 W were used to provide an overall etch rate of 0.21 μm/min and an aspect ratio of 7.7.

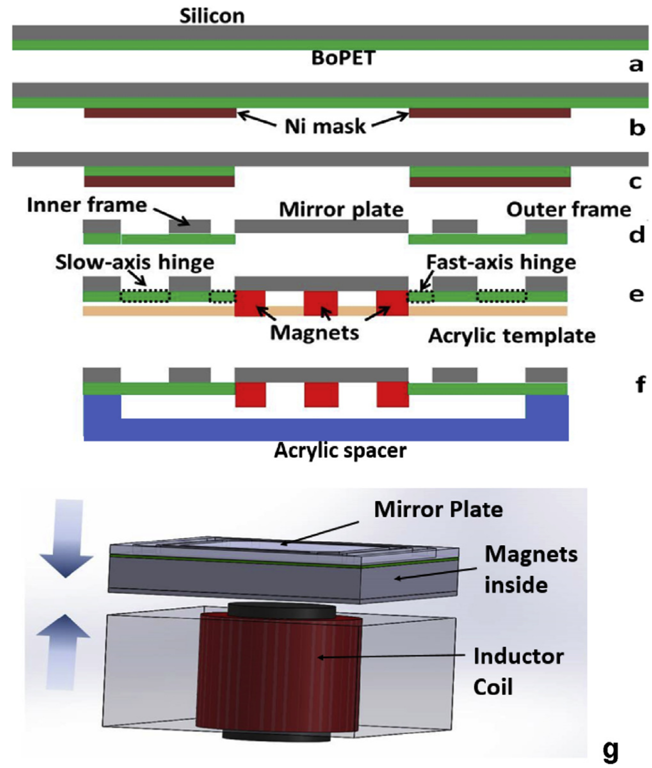

Fig. 8. The fabrication and assembly process.

Table 2
Etching Parameters for BoPET and Silicon.

	BoPET	Silicon
Temperature (°)	−80	−100
Pressure (mTorr)	30	30
Ar (sccm)	80	0
O_2 (sccm)	30	30
SF_6 (sccm)	0	90
RF power (W)	150	10
ICP power (W)	300	600
Etch rate (μm/min)	0.21	1
Aspect ratio	7.14	55

Fig. 8 illustrates the fabrication process flow of the scanning mirror. The etching parameters for BoPET and silicon are listed in Table 2. First, a 200-μm thick silicon wafer was bonded to a 50 μm thick BoPET film with epoxy (Fig. 8a). After evaporating a chrome/copper seed layer on the backside of BoPET film, a 5 μm thick nickel layer was electroplated to serve as a mask for BoPET etching (Fig. 8b). The BoPET film was etched with cryogenic plasma etching (Fig. 8c). After the BoPET etching and removing the Ni mask, a 0.4-μm thick aluminum layer was deposited on the silicon wafer as a mask for cryogenic plasma etching to form the mirror plate, inner frame and outer frame (Fig. 8d). Next, four permanent magnet discs were assembled onto the mirror plate simultaneously by using a thin acrylic template (Fig. 8e). The acrylic template was prepared with laser cutting. After the permanent magnets were securely bonded onto the mirror plate, the acrylic template was removed. Lastly, the fabricated mirror plate was bonded onto an acrylic spacer (Fig. 8f). The inductor coil was embedded into an acrylic holder. The acrylic spacer and holder were aligned and bonded together to complete the assembly of the mirror module (Fig. 8g). Fig. 9 shows a fully assembled scanning mirror with a zoom-in view of one BoPET hinge for the slow axis. It should be

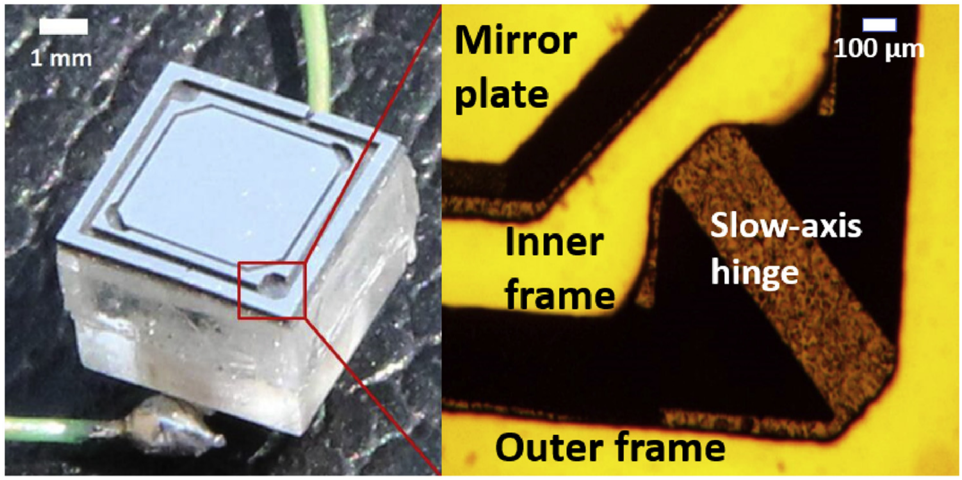

Fig. 9. An assembled prototype and zoom-in view of one slow-axis hinge.

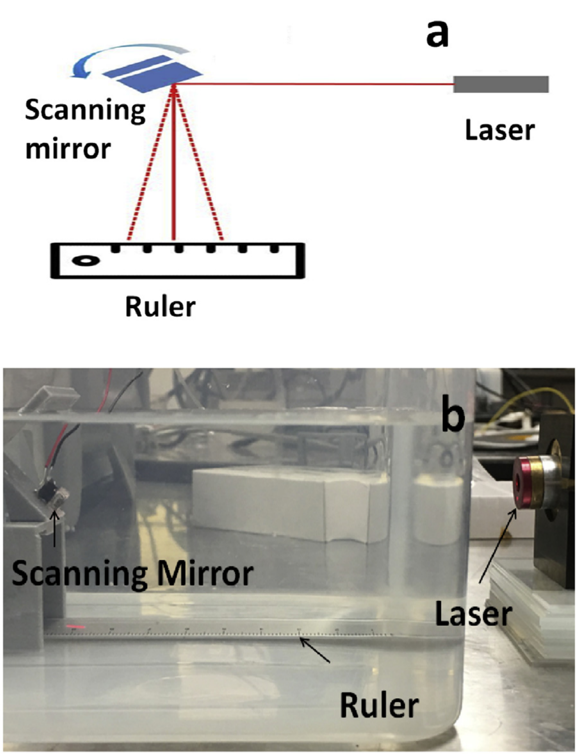

Fig. 10. (a) Laser tracing method (b) The testing setup.

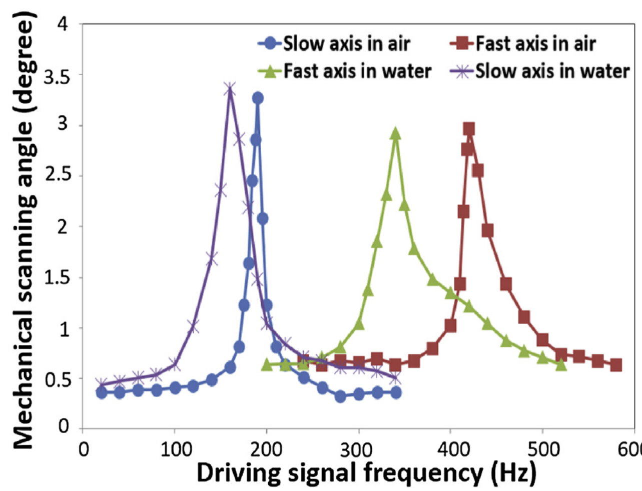

Fig. 11. Resonance frequency characterization of the fast and slow axes in the air and water.

noted that the acrylic spacer and holder can be replaced with a single piece of 3D printed structure to further simplify the assembly process.

4. Characterization

A laser tracing method was used to characterize the scanning performance of the water-immersible scanning mirror in both air and water. A collimated CW laser beam was incident on the center of the mirror pate at an incident angle of 45° and reflected vertically onto a ruler placed at certain distance away from the mirror plate. The tilting angle was calculated based on the length of the laser scanning trace on the ruler (Fig. 10).

The resonance frequencies of the fast and slow axes in the air and water were characterized. The amplitude of the AC driving currents for the fast and slow axes (in air) was set to be 100 mA and 30 mA, respectively. To overcome the stronger damping effect, the driving currents for the fast and slow axes (in water) were increased to 130 mA and 70 mA, respectively. To ensure the repeatability of the testing, the maximal tilting angle is limited to ±3.5° to avoid possible plastic deformation and degradation of the BoPET hinges due to excessive shear strain. With a proper setup, a ±3.5° scanning can provide a field of view of 1–3 mm, which should be adequate for many scanning microscopy modalities. Fig. 11 shows the tilting angles of the fast and slow axes at different driving frequencies. In air, the resonance frequencies of the fast and slow axes were determined to be 420 Hz and 190 Hz, respectively. The corresponding FWHM (full width at half maximum) around the two resonance frequencies is estimated to be 50 Hz and 20 Hz, respectively. When immersed in water, the resonance frequencies were reduced to 330 Hz and 160 Hz, respectively. The corresponding FWHM (full width at half maximum) around the two resonance frequencies is estimated to be 65 Hz and 25 Hz, respectively. In both cases, the measured resonance frequencies match well with the simulation results).

From Fig. 12, the quality factors of the fast and slow axes in air were determined (as the ratio between the resonance frequency and the FWHM) to be 8.4 and 9.5, respectively. In water, they were reduced to 5.1 and 6.4, respectively. Compared with the simulation results, the quality factors of both axes are lower (with larger

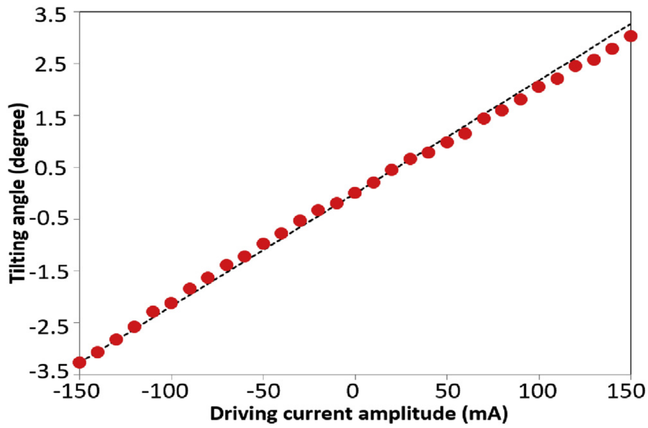

Fig. 12. DC driving test result of the slow axis; simulated results in dash lines.

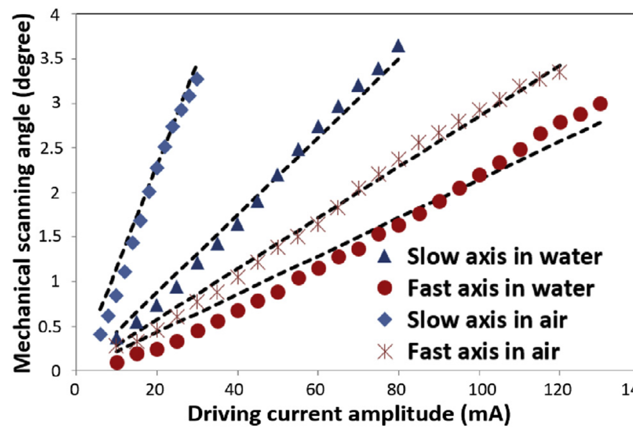

Fig. 13. Tilting angles at resonance frequencies; simulated results in dash lines.

FWHM). This is because only viscous damping was considered in the simulation. In real testing, there were other damping sources, such as viscoelastic damping in the BoPET hinges and electromagnetic damping due to current induction in the inductor coil, which will further reduce the quality factors. The low resonance frequency and quality factor of the slow axis allows it to be driven even at DC without using a driving current much higher than that at resonance frequency. This feature is especially useful in scanning optical and acoustic microscopy, where a dense line-by-line raster scanning pattern of the laser or ultrasound focal point can be achieved with a saw-tooth driving signal to enhance the lateral resolution. As shown in Fig. 12, the tilting angle of the slow axis increases almost linearly with the DC driving current, which matches well with the simulation results. In addition, the tilting angles of the fast and slow axes driven at their resonance frequencies were also characterized. As shown in Fig. 13, the tilting angles increases almost linearly with the driving current amplitude.

Raster scanning pattern in water with both axes actuated was also characterized. The fast-axis driving current was set to be 330 Hz, 130 mA to achieve a tilting angle of ±3°. The slow-axis driving currents were 110 Hz, 260 mA (Fig. 14a), 82.5 Hz, 350 mA (Fig. 14b), 66 Hz, 410 mA (Fig. 14c) and 55 Hz, 430 mA (Fig. 14d), respectively to maintain a similar tilting range. The maximum power consumption was determined to be 127 mW in air and 294 mW in water. Although the power is higher in water to overcome stronger damping effect, this should not be a problem due to much better cooling conditions. If necessary, the driving current and the power consumption can be reduced by using inductor coils with higher inductance and/or stronger permanent magnets.

5. Conclusion

A new micromachined two-axis water-immersible scanning mirror using BoPET hinges has been demonstrated. Miniaturization and batch fabrication of the mirror package is made possible with the development of a new micromachining process. The low stiffness of the torsional polymer hinges allows easy tuning of the resonance frequencies of the two scanning axes without drastically different geometries. The low quality factor of the resonance makes it possible to drive the scanning mirror efficiently at frequencies other than the resonance. Such feature is useful in creating desired raster scanning patterns for different scanning microscopic imaging applications.

Acknowledgments

This work was supported in part by a grant from the National Science Foundation (IDBR-1255921) and a Prematurity Research Center grant from the March of Dimes Foundation.

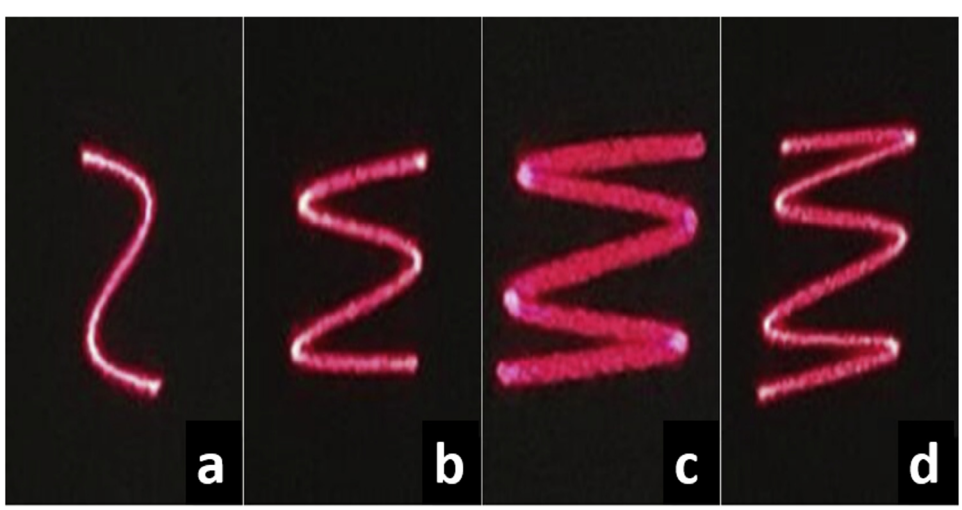

Fig. 14. Raster scanning patterns at different slow-axis scanning frequencies when scanning mirror immersed in water.

References

[1] X.Y. Zhang, Sj. Koppal, R. Zhang, L. Zhou, E. Butler, H.K. Xie, Wide-angle structured light with a scanning MEMS mirror in liquid, Opt. Express 24 (4) (2016) 3479–3487.
[2] J. Yao, C.H. Huang, L. Wang, J.M. Yang, L. Gao, K.I. Maslov, J. Zou, L.V. Wang, Wide-field fast-scanning photoacoustic microscopy based on a water-immersible MEMS scanning mirror, SPIE Journal of Biomedical Optics 17 (8) (2012), 080505.
[3] J.Y. Kim, C. Lee, K. Park, G. Lim, C. Kim, Fast optical-resolution photoacoustic microscopy using a 2-axis water-proofing MEMS scanner, Sci. Rep. 5 (1) (2015) 7932.
[4] K.E. Petersen, Silicon torsional scanning mirror, IBM J. Res. Dev. 24 (5) (1980) 631–637.
[5] D.L. Dickensheets, G.S. Kino, Micromachined scanning confocal optical microscope, Opt. Lett. 21 (10) (1996) 764–766.
[6] K.H. Gilchrist, D.E. Dausch, S. Grego, Electromechanical performance of piezoelectric scanning mirrors for medical endoscopy, Sens. Actuators A: Phys. 178 (5) (2012) 193–201.
[7] A.D. Yalcinkaya, H. Urey, D. Brown, T. Montague, R. Sprague, Two-axis electromagnetic microscanner for high resolution displays, IEEE J. Microelectromech. Syst. 15 (4) (2006) 786–794.
[8] S. Xu, C.H. Huang, J. Zou, A microfabricated water-immersible scanning mirror with a small form factor for handheld ultrasound and photoacoustic microscopy MOEMS and Miniaturized Systems XV, Vol. 9760, International Society for Optics and Photonics, 2016, 976002.
[9] S. Xu, J. Zou, Two-axis water-immersible microscanning mirror for scanning optics and acoustic microscopy, SPIE J. Micro/Nanolithogr., MEMS, and MOEMS 15 (4) (2016), 045005.
[10] P.E. Dyer, J. Sidhu, Excimer laser ablation and thermal coupling efficiency to polymer films, J. Appl. Phys. 57 (4) (1985) 1420–1422.
[11] P.E. Dyer, G.A. Oldershaw, J. Sidhu, CO 2 laser ablative etching of polyethylene terephthalate, Appl. Phys. B 48 (6) (1989) 489–493.
[12] A. Vesel, M. Kolar, A. Doliska, K. Stana-Kleinschek, M. Mozetic, Etching of polyethylene terephthalate thin films by neutral oxygen atoms in the late flowing afterglow of oxygen plasma, Surf. Interface Anal. 44 (13) (2012) 1565–1571.
[13] S. Xu, X. Duan, J. Zou, A two-axis water-immersible Micro scanning mirror driven by single inductor coil through dynamic structural filtering, Sens. Actuators A Phys. 284 (12) (2018) 172–180.
[14] Handbook P. (1989). Brandrup J., Immergut EH., Eds.
[15] P. Harinarayanan, U. Cvelbar, Selective plasma etching of polymeric substrates for advanced applications, Nanomaterials 6 (6) (2016) 108.

Biographies

Song Xu received his B.S. in optical and electrical engineering from Huazhong Univ. of Science and Technology, P. R. China (2012). He is currently pursuing the Ph. D. in the Department of Electrical and Computer Engineering at Texas A&M University. His current research involves building MEMS scanning mirrors for SAM and PAM and ultrasound image reconstruction.

Shuangliang Li received his B.S. in microelectronics science and engineering from East China Normal University in 2017. He is currently pursuing the Ph. D in the department of elctrical and computer engineering at Texas A&M University. His current research is mainly on MEMS scanning mirrors design and fabrication.

Jun Zoureceived his Ph.D. degree in electrical engineering from University of Illinois at Urbana-Champaign in 2002. In 2004, he joined in the department of electrical and computer engineering at Texas A&M University, where he is currently a full professor. His current research interests lie in the development of micro and nano opto-electro-mechanical devices and systems for biomedical imaging and sensing applications. He is a Senior Member of IEEE and SPIE, and a member of OSA.